NUMERICAL SIMULATION OF ELECTROSTATIC COUNTERSTREAMING INSTABILITIES IN ION BEAMS*

D. W. Forslund and C. R. Shonk
Los Alamos Scientific Laboratory, Los Alamos, New Mexico 87544
(Received 13 May 1970)

We report two-dimensional numerical studies of the nonlinear evolution of the electrostatic instabilities of two interpenetrating ion beams in an electron background, and comparison with the predictions of linear and quasilinear theory.

Linear theory.—The initial equilibrium consists of two relatively cold, equal-density, Maxwellian ion beams moving with velocity $\pm v_D$ in the x direction with respect to the electrons [Fig. 1(a)] which have an isotropic thermal velocity $v_e = (2T_e/m_e)^{1/2}$ which in all cases treated is larger than v_D. This equilibrium is unstable to two types of modes[1-3]: (1) ion-ion instabilities which have zero real frequency in the electron frame, and (2) electron-ion instabilities which have phase velocities situated between the electron and ion distribution functions. The regions of parameter space in which the two instabilities exist for a one-dimensional plasma are shown in Fig. 1(b) for $m_i/m_e = 25$. The points correspond to the simulations performed, with + denoting the two cases discussed here. Since the growth rate of the electron-ion instability increases monotonically with drift velocity, in two dimensions the most unstable modes will still be aligned with the flow direction. The cutoff in the ion-ion instability at an acoustic Mach number of 1 [$M = v_D/c_S$ where $c_S = (T_e/m_i)^{1/2}$], however, implies that for higher Mach numbers in two dimensions all unstable modes will occur at large angles to the flow direction. The electrostatic plasma dispersion relation has been solved numerically. Figure 1(c) shows contours of constant growth rate versus wave number for the ion-ion instability. The contours are spaced at intervals of $0.069\omega_{pi}$ from the outermost (zero-growth) contour; the maximum growth rate is $0.309\omega_{pi}$. The electron-ion growth contours, Fig. 1(d), are spaced at intervals of $0.021\omega_{pi}$ with a maximum growth rate of $0.187\omega_{pi}$.

Quasilinear theory.—We can describe at least the initial nonlinear evolution of the system by the two-dimensional quasilinear equations.[4] The jth-component spatially averaged distribution function $f_j(\vec{v}, t)$ evolves according to

$$\frac{\partial f_j}{\partial t} = \frac{\partial}{\partial \vec{v}} \cdot \overleftrightarrow{D}_j \cdot \frac{\partial f_j}{\partial \vec{v}}, \tag{1}$$

where the diffusion tensor is given by

$$\overleftrightarrow{D} = \frac{e^2}{m^2} \sum_{k>0} |E_k|^2 \frac{\hat{k}\hat{k}\gamma_k}{(\vec{k}\cdot\vec{v})^2 + \gamma_k^2}. \tag{2}$$

We include only the zero-frequency growing ($\gamma_k > 0$) ion-ion modes and combine modes with positive and negative k (the electron-ion modes are treated adequately by the one-dimensional equations).[5] The usual adiabatic condition $\gamma_k/\omega_k < 1$ is replaced by $\gamma_k/kv_T < 1$[6] where v_T is a characteristic speed for each species (v_e for electrons and v_D for ions). The energy density $W_k(t) = |E_k|^2/8\pi$ in electric field fluctuations evolves according to $(\partial/\partial t)W_k(t) = 2\gamma_k W_k(t)$ and $\gamma_k(t)$ is determined in terms of $f_j(\vec{v}, t)$ from the linear dispersion relation. For comparison with the simulation, we take velocity moments of Eq. (1) and use the wavelength for the maximum growth rate from Fig. 1(b) to estimate the integrands in the

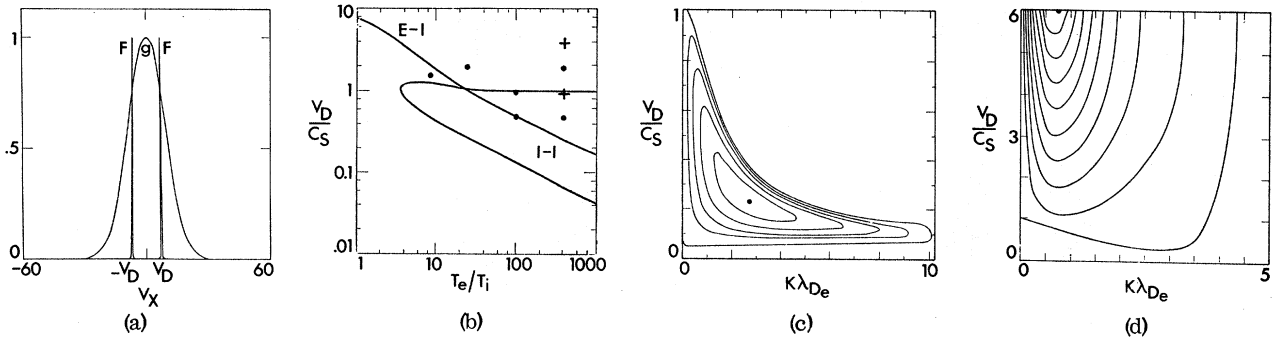

FIG. 1. (a) Initial ion and electron v_x distribution functions, (b) stability boundaries, and growth rate contours of (c) the ion-ion and (d) electron-ion instability for $m_i/m_e = 25$, $T_e/T_i = 400$.

quasilinear equations to obtain initially for each ion beam

$$\frac{nm_i}{2}\frac{dv_D^2}{dt}\sim-\frac{1}{2}\frac{1}{\alpha^2M^2}\frac{dW_F}{dt}, \tag{3}$$

$$\frac{nm_i}{2}\frac{d}{dt}\langle v_y^2\rangle_i\sim\frac{1}{2}\frac{1-\alpha^2}{\alpha^2M^2}\frac{dW_F}{dt}, \tag{4}$$

$$\frac{nm_i}{2}\frac{d}{dt}\langle(v_x-v_D)^2\rangle_i\sim\frac{1}{2M^2}\frac{dW_F}{dt}, \tag{5}$$

where $\alpha=k_x/k$ and $W_F=\sum_k W_k$. In our simulations $\alpha\sim 1/3M$ for the fastest growing mode.

Equations (3), (4), and (5) indicate that the x and y thermal energies of the ion beams increase at the expense of the ion-beam kinetic energy, with the y energy increasing faster than the x energy by $(1-\alpha^2)/\alpha^2$. The quasilinear equations also show that the ions gain energy until $\langle(v_x-v_D)^2\rangle\sim 2\alpha^4v_D^2/(1+\alpha^2)$ and $\langle v_y^2\rangle\sim\alpha^2v_D^2/(1+\alpha^2)$ so that the final ion-temperature anisotropy is $T_f^y/T_f^x\sim 2\alpha^2$. For high Mach numbers the final y temperature is $T_f^y\sim T_e/4$. The fractional change in beam velocity is $\Delta v_D/v_D(0)\sim\alpha^2$.

Numerical simulation.—A two-dimensional particle-in-cell computer program has been developed to simulate the electrostatic interaction of electrons and ions. The model is similar to that of Morse and Nielson.[7] Each of the ion and electron species is represented by 90 000 simulation points which move in a square, 64×64, doubly periodic mesh. To reduce the initial thermal fluctuation level, the ions and electrons are initially distributed uniformly in x and y.

To assess the validity of this technique, simulations of stable two-ion-beam plasmas for 1000 time steps, to $t=50\tau_{pe}$, have been carried out at $T_e/T_i=3$, $M=1$, with relevant lattice spacings. Energy is conserved to better than 0.5% and the beams have been slowed by less than 1.2%.

Figures 2 and 3 show representative results for $T_e/T_i=400$, acoustic Mach numbers 1 and 4, respectively. Note that neither case is unstable in one dimension, i.e., in x alone. In all figures, lengths are measured in electron Debye lengths, λ_{De}; times in electron plasma periods, $\tau_{pe}=2\pi/\omega_{pe}$; and velocities in units of $v_0=\lambda_{De}/\tau_{pe}$. As a result of this scaling, the electron thermal velocity has the constant value $v_{th}{}^e=2\pi\sqrt{2}$. The symbol U denotes velocity components along the streaming direction, x; and V denotes velocity in the transverse direction, y. Distribution functions of ion v_x, $f_i(v_x)$, are labeled F, and ion v_y distribution functions, $f_i(v_y)$, are labeled G. The corresponding electron distribution functions, $f_e(v_x)$, $f_e(v_y)$, are labeled f and g. For

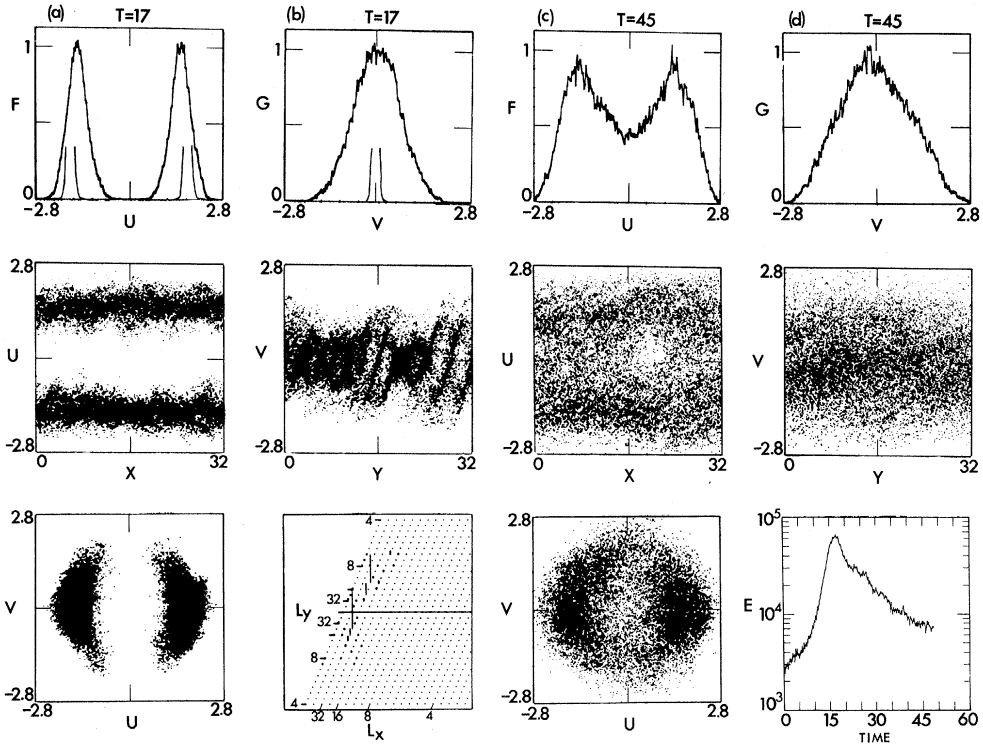

FIG. 2. Two-ion-beam simulation, $M=1$, $T_e/T_i=400$.

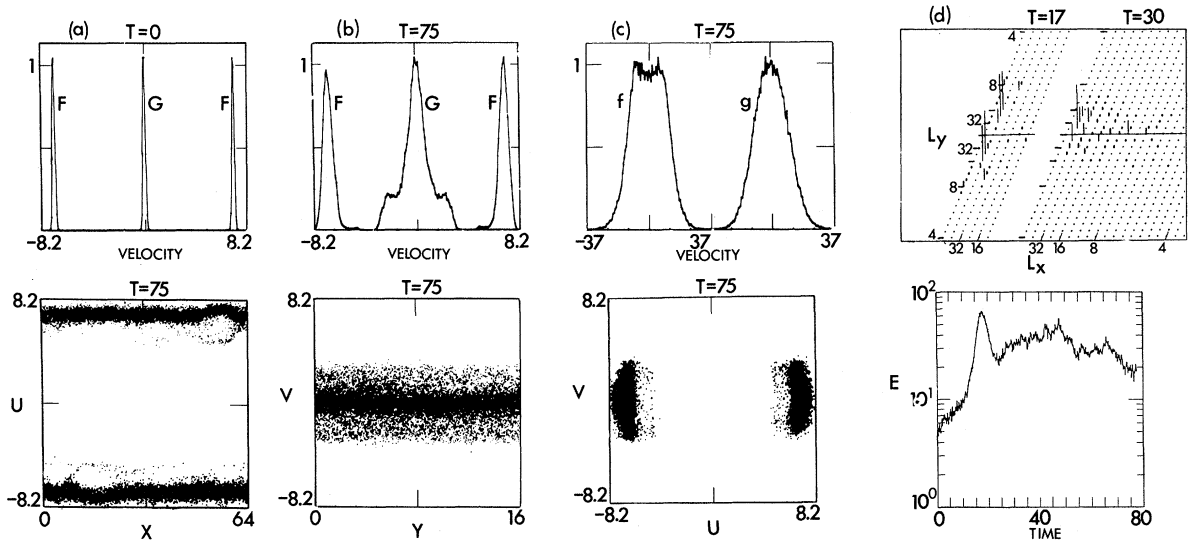

FIG. 3. Two-ion-beam simulation, $M=4$, $T_e/T_i=400$.

clarity, distribution functions are normalized so that peak values are unity and hence the area under the functions is not constant.

Ion distribution functions for the case $M=1$ are shown in the top row of Fig. 2. Columns (a) and (b) refer to the time of maximum field energy, i.e., saturation, $t=17\tau_{pe}$. The initial ion distributions are indicated by broken lines. The electron distributions are essentially unchanged, and are not shown. Due to the strong ion-ion instability, the average drift speed of each beam has decreased by 12%, and the ion beams are heated differently in x and y, resulting in $T_e/T_i^x \sim 33$, $T_e/T_i^y \sim 6.5$, in agreement with quasilinear theory. Phase-space plots are shown in the middle row. At the bottom of Fig. 2(a), a plot of v_y vs v_x for the ions is shown.

A Fourier-mode analysis of the electric field energy is shown in Fig. 2(b), bottom. The length of the vector attached to a given mode is proportional to the energy in that mode. The numbers on the axes indicate the wavelengths of the modes in cell units, i.e., the inverse lattice space of the computing grid, which when mulitplied by the lattice spacing, $\Delta x=\Delta y=0.5$, give wavelengths in λ_{De}. We see that at saturation, the predominant modes grow at about 60° to the drift axis with wavelengths $L_x \sim 16\lambda_{De}$ and $L_y \sim (5\text{-}8)\lambda_{De}$. These modes are not the fastest growing modes for $T_e/T_i=400$, but those corresponding to a reduced value of T_e/T_i.

Figures 2(c) and 2(d) show the situation well after the decay of the instability, $t=45\tau_{pe}$. The ion beams have been heated so much that the beam structure is nearly destroyed. The phase-space diagrams, Fig. 2(c) and 2(d), middle, show that the fine instability structure present at saturation has dissipated. The velocity space plot, Fig. 2(c), bottom, illustrates that the effect of the instability is to smear out the ions to approximately equal temperatures in both directions. The electron-ion temperature ratio is now so low that the instability is turned off. The electrons remain adiabatic.

Figure 2(d), bottom, the logarithm of total field energy plotted against time, shows an exponential growth between $t=7\tau_{pe}$ and $15\tau_{pe}$. The rate is somewhat slower than that predicted by linear theory, Fig. 1(b), but in good agreement with linear theory for the mixture of waves existing at saturation, Fig. 2(b), bottom.

Figure 3 shows $M=4$ results; to accommodate the strongly off-angle instabilities, the mesh spacing is $\Delta x=1$, $\Delta y=\frac{1}{4}$. Initial ion velocity distributions in v_x and v_y are shown in Fig. 3(a), top. For the low simulation mass ratio, $m_i/m_e=25$, both the ion-ion and ion-acoustic instabilities are present, but have different behaviors. The ion-ion instability grows nearly perpendicularly to the drift direction. That is, $k_y \gg k_x$. The quasilinear results described above for the ion-ion instability indicate only slight heating of the ions in x, but a large heating in y. This situation is apparent in the ion distribution functions at late time, $75\tau_{pe}$, shown in Fig. 3(b), top. The "shoulders" on G, i.e., $f_i(v_y)$, are characteristic of the large-M ion-ion instability and are caused by a resonant trapping interaction of

the dominant narrow band of $k_y \gg k_x$ modes with the tails of $f_i(v_y)$ when the velocity spread in v_y has nearly increased to the cutoff condition.

Electric field energy modes are shown in Fig. 3(d), top. At the left in this figure, the ion-ion saturation-time modes indicate growth at above 85° to the flow direction, at wavelengths $L_x \sim 64\lambda_{De}$ and $L_y \sim 6\lambda_{De}$. The ion-ion instability decays rapidly, and at the right, $t = 30\tau_{pe}$, the Fourier plot shows growing parallel modes of the ion-acoustic instability having wavelengths near $10\lambda_{De}$ (in agreement with linear theory) and decaying off-axis ion-ion modes at longer wavelengths.

Ion phase- and velocity-space plots at $75\tau_{pe}$ are given in Figs. 3(a), 3(b), and 3(c), bottom. The ion-acoustic instability structure can be seen on the slightly v_x-broadened ion beams. Electron distribution functions at $75\tau_{pe}$ are shown in Fig. 3(c), top. The electron v_x distribution, f, has broadened by 15% and is flat-topped. By flattening the electron distribution in the region between the beams, the resonant ion-acoustic instability is shut off. The electron v_y distribution function, g, has also been broadened to nearly the same spread as v_x.

It seems clear that when electron thermal velocities are much larger than ion velocities, the electrons act only as a charged fluid with pressure, and in fact the linear theory of the ion-ion instability is essentially based on such a view of the electrons. Hence cold electrons adiabatically tied to a magnetic field should produce the same effect and have been observed to do so in other simulations at large Alfvén Mach numbers, which showed strong $k_y \gg k_x$ modes[8] which have been referred to as "Venetian blinds."

All cases run inside the one-dimensional instability region, Fig. 1(b), showed even stronger interaction between the two ion beams than in the $M = 1$ case, Fig. 2. The transition between strong interaction, Fig. 2, and weak interaction, Fig. 3, occurs just above $M = 1$.

*Work performed under the auspices of the U. S. Atomic Energy Commission and the Defense Atomic Support Agency.

[1]T. E. Stringer, J. Nucl. Energy, Part C 6, 267 (1964).

[2]B. D. Fried and A. Y. Wong, Phys. Fluids 9, 1084 (1966).

[3]T. Ohnuma and Y. Hatta, Kakuyugo-Kenkyu 15, 637 (1965), and 16, 95 (1966).

[4]I. B. Bernstein and F. Englemann, Phys. Fluids 9, 937 (1966).

[5]R. C. Davidson, N. A. Krall, K. Papadopoulos, and R. Shanny, Phys. Rev. Lett. 24, 579 (1970).

[6]V. D. Shapiro and V. I. Shevchenko, Zh. Eksp. Teor. Fiz. 45, 1612 (1963) [Sov. Phys. JETP 18, 1109 (1964)].

[7]R. L. Morse and C. W. Nielson, Phys. Rev. Lett. 23, 1087 (1969).

[8]R. L. Morse and C. R. Shonk, in European Space Research Organization Report No. SP-51, 1969 (unpublished).

TRAPPING OF POSITRONS AT VACANCIES IN METALS*

C. H. Hodges
Queen's University, Kingston, Ontario, Canada
(Received 19 May 1970)

Measurements of the lifetime for positron annihilation in metals show a temperature dependence which has been ascribed to the trapping of positrons at vacancies. An explanation of this trapping process is presented in terms of an effective potential well, whose depth is the difference between the bottom of the positron energy band in the solid and the potential felt by the positron inside the vacancy.

For some time now it has been known that positron annihilation rates or lifetimes in many metals show a dependence on temperature of the sort illustrated in Fig. 1, for Al and In. This effect was first reported by Mackenzie et al.,[1] who ascribed it to increasing vacancy concentration with rise in temperature. A vacancy represents the absence of a positive ionic charge from the host lattice and is therefore attractive to a positron but repulsive to an electron. With increasing vacancy concentration the electron-positron wave-function overlap decreases and the annihilation rate goes down. The curve for Al in Fig. 1 flattens out again at higher temperatures where by conventional estimates the vacancy concentration is still only 1 in 10^5. At concentrations greater than this, all annihilation must be taking place at or very near vacancies, and this strong-